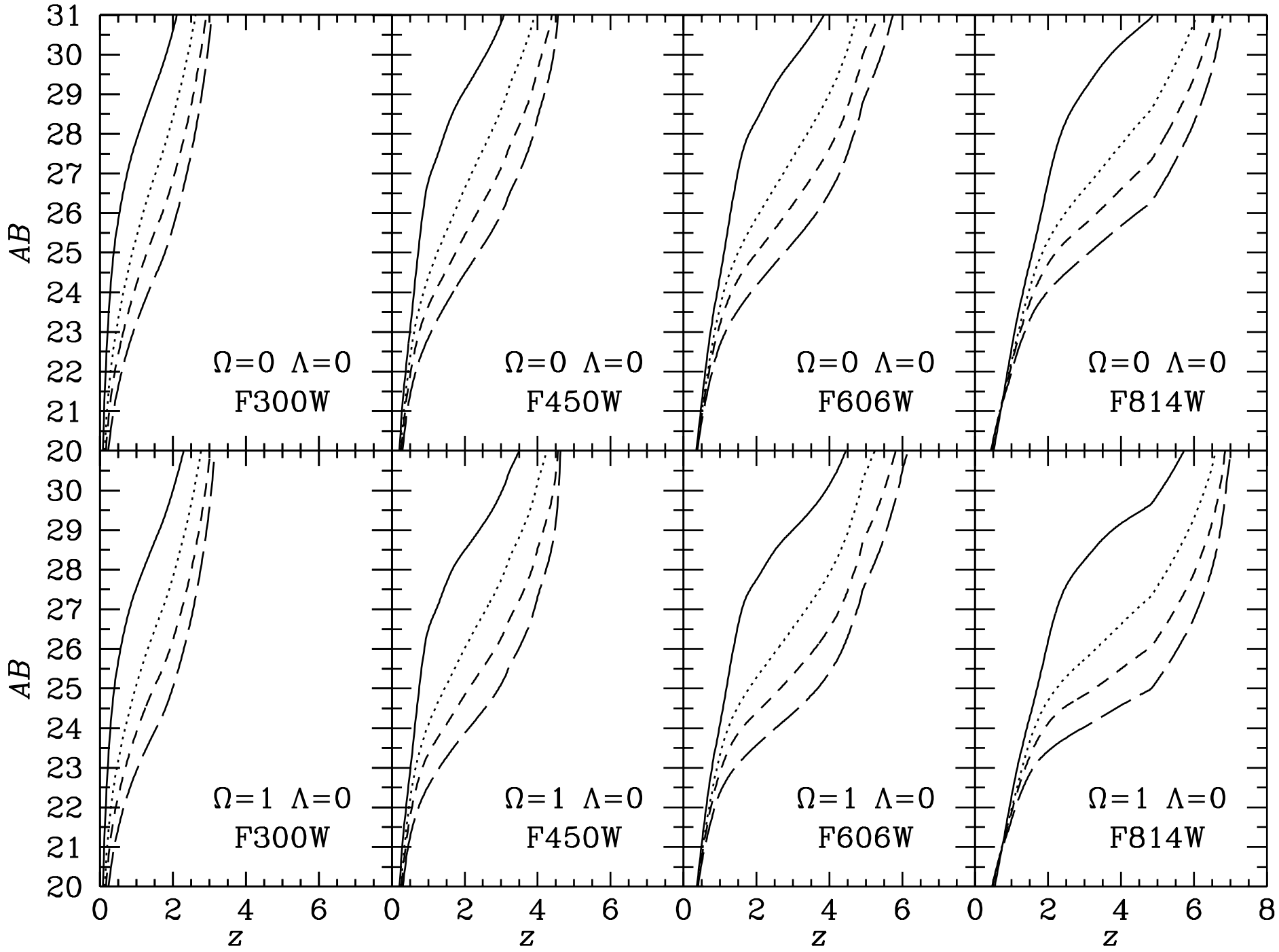
Ω=0 Λ=0
F300W
Ω=0 Λ=0
F450W
Ω=0 Λ=0
F606W
Ω=0 Λ=0
F814W
Ω=1 Λ=0
F300W
Ω=1 Λ=0
F450W
Ω=1 Λ=0
F606W
Ω=1 Λ=0
F814W
AB
z

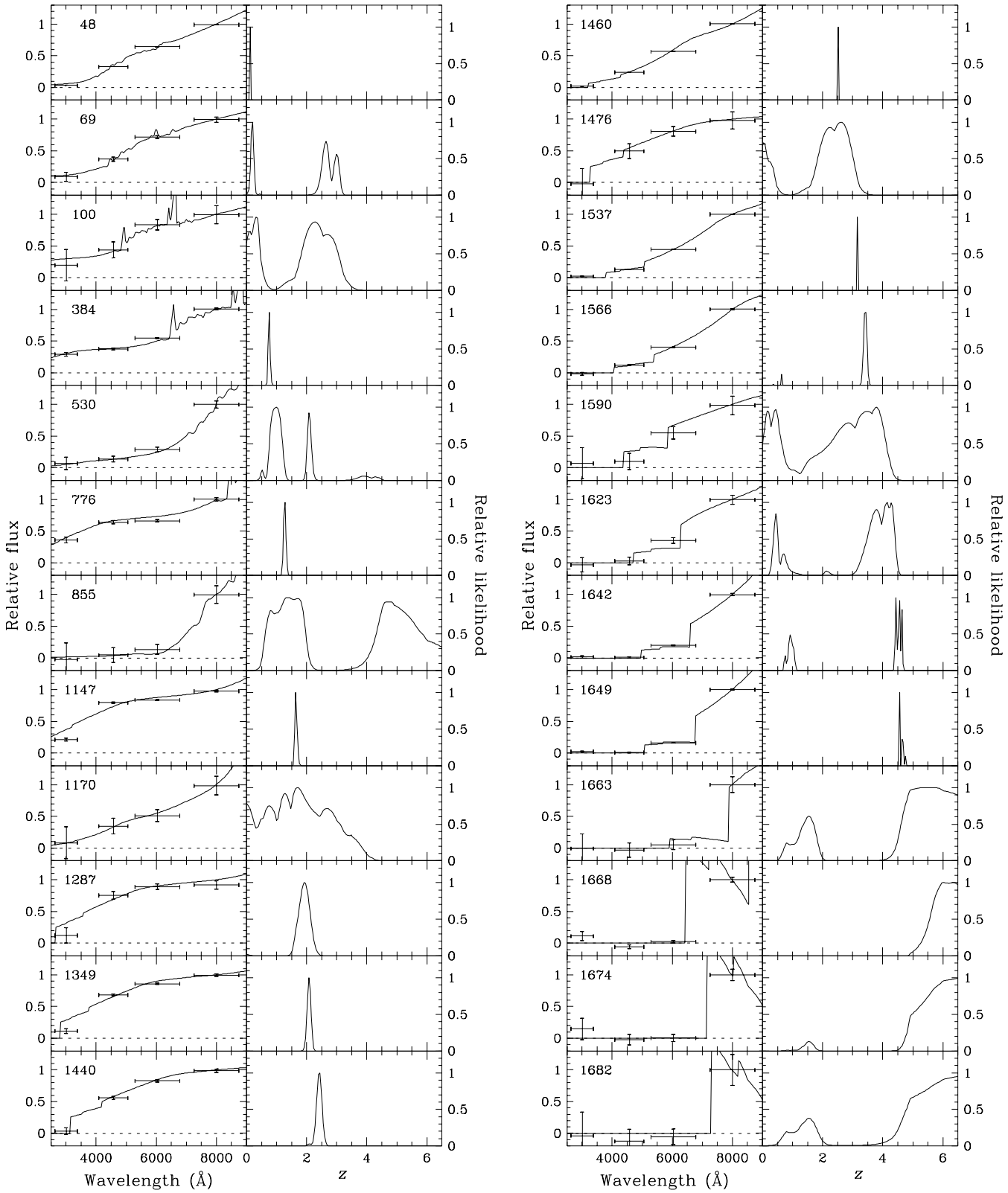
48
69
100
384
530
776
855
1147
1170
1287
1349
1440
1460
1476
1537
1566
1590
1623
1642
1649
1663
1668
1674
1682
Relative flux
Relative likelihood
Wavelength (Å)
z

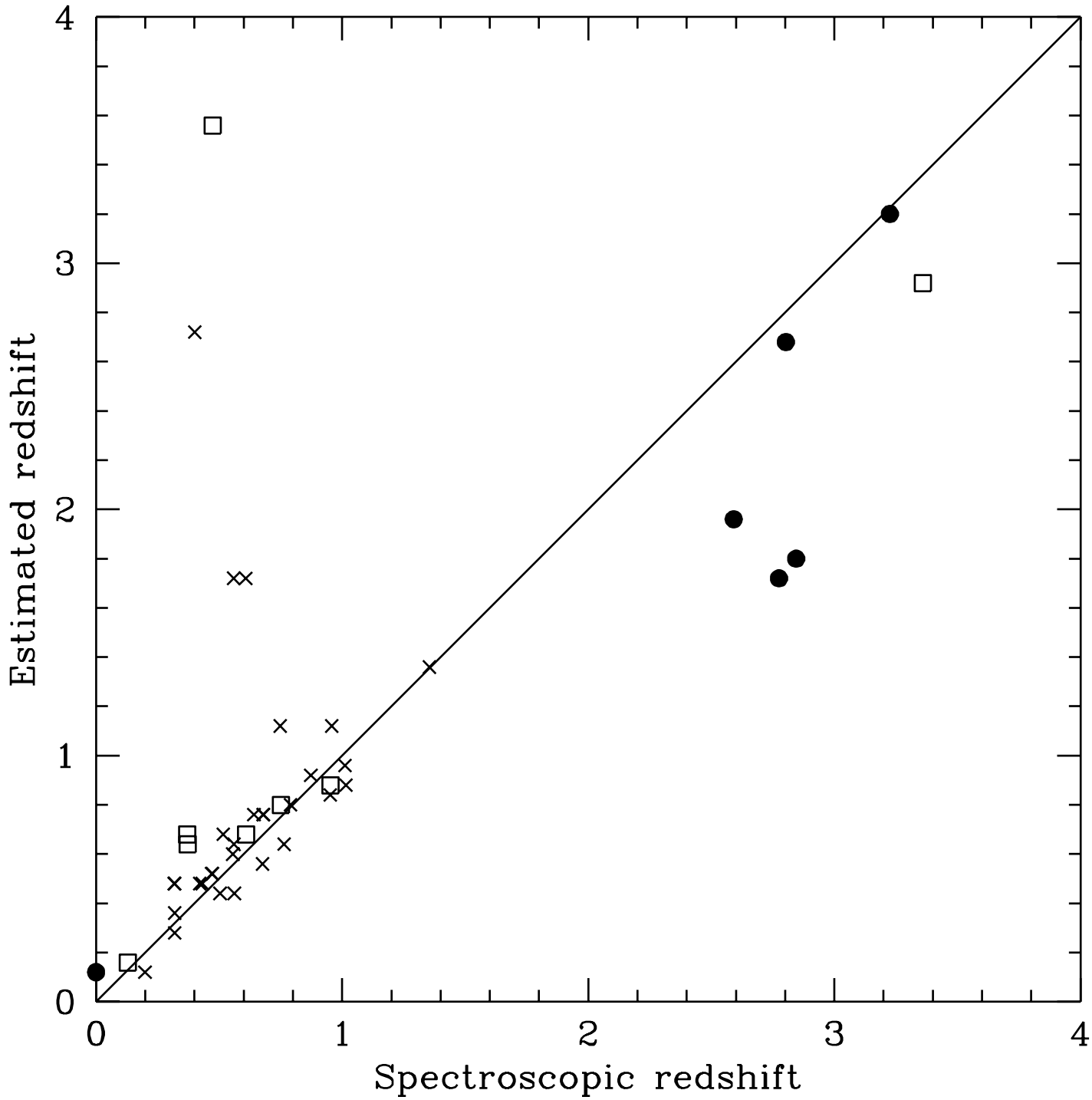
Estimated redshift
Spectroscopic redshift
0
1
2
3
4

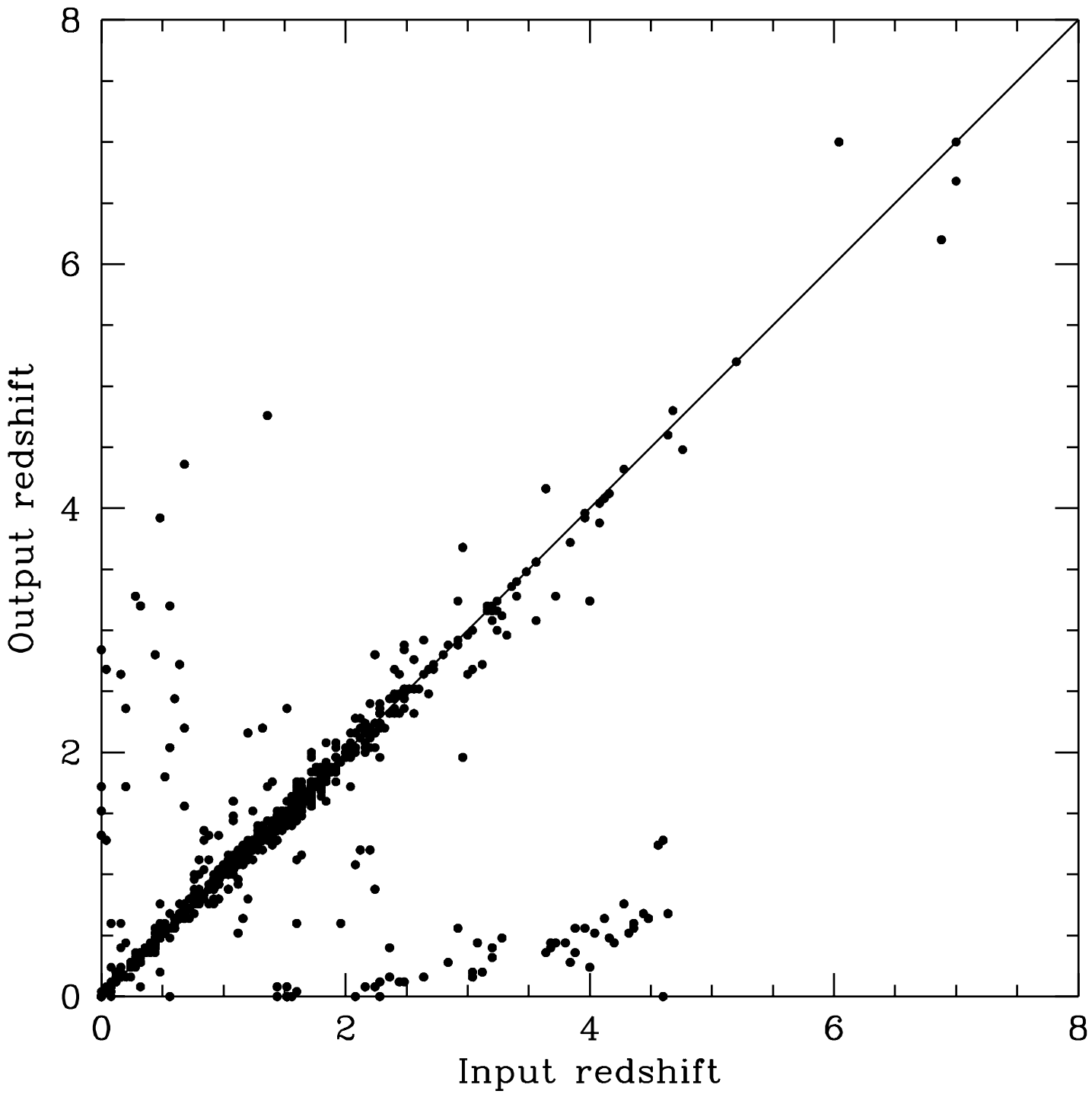
Output redshift
Input redshift
0
2
4
6
8

arXiv:astro-ph/9606171v1 27 Jun 1996

# Star-forming galaxies at very high redshifts

**Kenneth M. Lanzetta[1], Amos Yahil[1] & Alberto Fernández-Soto[2,3]**

[1]Astronomy Program, Department of Earth and Space Sciences, State University of New York at Stony Brook, Stony Brook, NY 11794–2100, USA

[2]Instituto de Física de Cantabria, Consejo Superior de Investigaciones Científicas, [3]Departamento de Física Moderna, Universidad de Cantabria, Facultad de Ciencias, 39005 Santander, SPAIN

**Analysis of the deepest available images of the sky, obtained by the Hubble Space Telescope, reveals a large number of candidate high-redshift galaxies. A catalogue of 1,683 objects is presented, with estimated redshifts ranging from $z = 0$ to $z > 6$. The high-redshift objects are interpreted as regions of star formation associated with the progenitors of present-day normal galaxies at epochs reaching to 95% of the time to the Big Bang.**

The longstanding effort to identify normal galaxies at high redshifts has undergone dramatic progress in recent months. New observations by Steidel et al.[1] to magnitude $AB(6930) < 25$ (where $AB(\lambda)$ is the monochromatic magnitude at wavelength $\lambda$) have revealed a population of galaxies at redshift $z \approx 3$ and have demonstrated that the Lyman-limit spectral discontinuity and Ly$\alpha$-forest spectral decrement, which arise owing to photoelectric absorption by neutral hydrogen along the line of sight, together constitute the most prominent spectral signature of very distant galaxies. This result has two important implications. First, it provides a means of identifying high-redshift galaxies. The spectra of high-redshift galaxies are characterized by (1) a complete absence of flux below the Lyman limit and (2) strongly absorbed flux in the Ly$\alpha$ forest. This spectral signature is observable by means of broad-band photometry and must apply irrespective of the underlying spectral properties of the galaxies because it is imprinted by intervening rather than intrinsic material. Second, it allows high-redshift interpretations of low-redshifts galaxies to be excluded. The rate of incidence of high-redshift Lyman-limit and Ly$\alpha$-forest absorbers is sufficiently large that stochastic variations between different lines of sight are essentially negligible. High-redshift galaxies must exhibit the spectral signature of Lyman-limit and Ly$\alpha$-forest absorption, and any observation to the contrary is sufficient to rule out the possibility of a high redshift.

The Hubble Deep Field (HDF) images, obtained by the Hubble Space Telescope (HST) in December 1995, permit a search for the spectral signature of Lyman-limit and Ly$\alpha$-forest absorption to magnitudes far fainter than were previously accessible. The images were obtained with the Wide Field Planetary Camera 2 (WFPC2) through four filters spanning near-ultraviolet through near-infrared wavelengths to a roughly uniform detection limit approaching $AB = 30$. The images are in principle sensitive to galaxies at redshifts as large as $z \approx 7$, beyond which the Lyman limit is redshifted past the response of the WFPC2 filters.

We have estimated redshifts of a large number of galaxies in the HDF images by fitting galaxy

spectral energy distributions, including the effects of intervening Lyman-limit and Ly$\alpha$-forest absorption, to precise photometry of objects detected in the images. Here we describe the analysis and present a catalogue of 1,683 objects of magnitude $AB(8140) \lesssim 30$ at estimated redshifts ranging from $z = 0$ to $z > 6$. The catalogue is essentially complete for magnitudes $AB(8140) < 28$ (1,104 objects), at which 367 objects are at estimated redshift $z = 0 - 1$, 512 objects are at $z = 1 - 2$, 135 objects are at $z = 2 - 3$, 54 objects are at $z = 3 - 4$, 30 objects are at $z = 4 - 5$, two objects are at $z = 5 - 6$, and four objects are at $z > 6$. Even if the high-redshift identifications are incorrect, we show by simulations that most real galaxies of those magnitudes and redshifts would be detected and hence that the surface densities we find represent strict upper limits to the actual surface densities. The rapid decline in the number of objects at estimated redshift $z > 2$ is therefore significant and tightly constrains models of galaxy formation and evolution (A.Y., K.M.L., A. Campos, and A.F.-S., manuscript in preparation).

If the estimated redshifts are approximately correct, then the high-redshift objects typically have ultraviolet luminosities $\sim 10^9 - 10^{10}$ times the solar luminosity $L_\odot$, sizes $\sim 1$ kpc, and co-moving spatial densities that vary between 0.05 and 0.01 Mpc$^{-3}$ at redshifts between $z = 2.5$ and $z = 6$. The ultraviolet luminosities and sizes are similar to those of nearby starbursting galaxies, while the co-moving spatial densities are comparable to that of present-day galaxies. (Throughout we adopt a Hubble constant $H_0 = 100$ km s$^{-1}$ Mpc$^{-1}$ and an Einstein–de Sitter cosmology with $\Omega = 1$ and $\Lambda = 0$.) We interpret these objects as galactic or proto-galactic regions of star formation associated with the progenitors of present-day normal galaxies.

## Object detection

The first goal of the analysis is to detect objects in the F814W images and to measure their spectral energy distributions in the F300W, F450W, F606W, and F814W images. (The spectral sensitivities of these images peak at roughly 3000 Å, 4500 Å, 6060 Å, and 8140Å, respectively.)

First, we obtained and processed the HDF images (produced by the Version 2 drizzle algorithm) made available to the HST archive on February 29, 1996. We considered only the Wide Field Camera images, which are significantly deeper than the Planetary Camera images. We trimmed the images to include only columns and rows 191 through 1970 (because the images are of inferior quality at the edges) and eliminated deviant pixels by setting the value of any pixel that differed by more than $3\sigma$ from a local $3 \times 3$ pixel median equal to that median (because the images contain a number of single-pixel positive noise spikes or hot pixels). The angular extent of each trimmed image is $71.2 \times 71.2$ arcsec$^2$, and the total angular area covered by the trimmed images is 4.22 arcmin$^2$.

Next, we detected objects in the F814W images using the SExtract program[2]. The object detection criteria can be set in different ways for different purposes, and we adopted a conservative approach with the aim of achieving high reliability. Specifically, we changed the default parameters

of the program by: (1) smoothing the images by a Gaussian filter of FWHM = 0.12 arcsec (approximately the width of the point spread function) to aid the detection of faint sources,[3] (2) adopting a detection threshold of at least 10 contiguous pixels with signal-to-noise ratio $> 1.4$ each, and (3) eliminating objects that are close to other objects by setting CLEAN_PARAM = 2.0. Criterion (2) is equivalent to a surface brightness limit $\mu_{AB(8140)} < 26.1$ arcsec$^{-2}$ over a minimum area of 0.016 arcsec$^2$, which corresponds to an isophotal limiting magnitude of $AB(8140) = 30.6$. A total of 1,683 objects were detected, the faintest of which is of total magnitude $AB(8140) = 30.0$.

Next, we tested the completeness of the catalogue by re-applying the detection algorithm for different values of the smoothing and thresholding parameters. The object list does depend on these parameters, but for objects of magnitude $AB(8140) < 28$ we found less than 1% variation for any plausible choices of the parameters. We conclude that the catalogue is essentially complete to magnitude $AB(8140) < 28$.

Next, we determined the local covariance and background surrounding each object in the images. We considered a square region of at least $41 \times 41$ pixels surrounding each object (larger regions for larger objects) and excluded pixels associated with any object before measuring the local covariance and background. The local covariances must be used to determine accurate photometric uncertainties because the drizzled HDF images are significantly correlated over adjacent pixels ($\approx 40\%$ with immediate neighbors, $\approx 10\%$ with diagonal neighbors, and less at larger separations).

Last, we measured the spectral energy distribution of each object detected in the images. We used SExtract segmentation maps to identify the nonoverlapping pixels associated with each object and measured the flux of each object in each of the four images within its unique segmentation aperture. The choice of identical apertures in the four images assures that exactly the same portion of each object is measured in each image, which is essential for establishing meaningful spectral energy distributions. We subtracted the local background (which was generally negligible) and used the local $3 \times 3$ covariance matrices (between each pixel and its immediate and diagonal neighbors) to determine the photometric uncertainties.

## Redshift determination

The second goal of the analysis is to estimate redshifts of all objects by comparing measured and modelled spectral energy distributions.

First, we modelled spectral energy distributions of galaxies at redshifts $0 < z < 7$. We adopted the galaxy spectra (E/S0, Sbc, Scd, and Irr galaxies) of Coleman, Wu, & Weedman[4], extrapolating at wavelengths less than 1400 Å using results of Kinney et al.[5]. We chose not to apply evolutionary corrections to these spectra because such corrections are uncertain and because the adopted galaxy spectra already span a wide range of spectral properties. We incorporated the effects of intrinsic and intervening Lyman-limit absorption by assuming that galaxies are optically thick to ionizing radiation. This assumption has recently been verified by Leitherer et al.[6] for nearby

star-forming galaxies, but in any case the mean free path for intervening Lyman-limit absorption is sufficiently small[8] to make this assumption valid at all but the lowest redshifts ($z \approx 2.3$) for which the Lyman limit is of interest. We accounted for intervening Ly$\alpha$ and Ly$\beta$ absorption by applying measurements of Madau[8] and unpublished measurements of J. Webb of the Ly$\alpha$-forest flux decrement parameters $D_A$ and $D_B$. These measurements extend over the redshift range $0 < z < 5$ and were extrapolated to $z = 7$ using a simple fit. We integrated the redshifted spectra with the throughputs of the F814W, F606W, F450W, and F300W filters (including system throughputs) to derive the model spectral energy distributions. Figure 1 shows the expected $AB$ magnitudes (of the four galaxy types) through the WFPC2 filters of a galaxy of absolute magnitude $M_{AB(4500)} = -20$. We also modelled the spectral energy distribution of an M star using the spectrum of Jacoby, Hunter, & Christian[10], extrapolating at wavelengths longward of 7500 Å using our own observations.

Next, we constructed redshift likelihood functions of all objects in the images by comparing measured and modelled spectral energy distributions. Assuming that flux uncertainties are normally distributed, the likelihood $L(z,T)$ of obtaining measured fluxes $f_i$ with uncertainties $\sigma_i$ given modelled fluxes $F_i(z,T)$ at an assumed redshift $z$ for spectral type $T$ and normalization $A$ over the four filters $i = 1 - 4$ is

$$L(z,T) = \prod_i \exp\left\{-\frac{1}{2}\left[\frac{f_i - AF_i(z,T)}{\sigma_i}\right]^2\right\}. \quad (1)$$

For each object, we maximized Equation (1) with respect to spectral type and normalization to determine the redshift likelihood function $L(z)$ and maximized $L(z)$ with respect to redshift to determine the maximum-likelihood redshift estimate. We did not attempt to assign relative abundances to the different spectral types as functions of redshift but simply gave all types equal weight in the redshift likelihood functions.

The result of the analysis is a redshift likelihood function and maximum-likelihood redshift estimate of each of the 1,683 objects detected in the images. Spectral energy distributions and redshift likelihood functions of a representative sample of the objects are shown in Fig. 2, and surface densities of the objects as functions of redshift and limiting magnitude are given in Table 1. The complete catalogue of objects, as well as their spectral energy distributions and redshift likelihood functions are abailable as Supplementary Information, together with optimally added composite spectral energy distributions of the objects. The spectra of the objects fall into distinct classes depending on the estimated redshift. At redshift $z \lesssim 2.3$ the spectra exhibit no significant absorption by intervening material and are similar to the redshifted spectra of present-day galaxies. At redshift $2.5 \lesssim z \lesssim 4$ the spectra are characterized by strong flux in the F814W and F606W images, detectable flux in the F450W images, and no detectable flux in the F300W images. At redshift $4 \lesssim z \lesssim 5.5$ the spectra are characterized by strong flux in the F814W images, detectable flux in the F606W images, and no detectable flux in the F450W and F300W images. Finally, at redshift $z \gtrsim 6$ the spectra are characterized by strong flux in the F814W images and no detectable flux in the F606W, F450W and F300W images.

## Confirming and corroborating evidence

Several lines of evidence support the redshift estimates obtained by the analysis.

The redshift estimates are in good agreement with the spectroscopic redshifts recently reported by Steidel et al.[10] for six high-redshift objects, by Cowie[11] for 30 medium-redshift objects, and by Moustakas et al.[12] for eight medium- and high-redshift objects, as is illustrated in Fig. 3. Of the 44 objects, three high-redshift galaxies have redshifts underestimated by $\Delta z \approx 1$ due to confusion with the UV emission of other faint sources, and four bright medium-redshift objects, of magnitudes $AB(8140) = 20.5 - 22.8$, have redshifts overestimated by $\Delta z > 1$ because the uncertainties used in Equation (1) do not include the cosmic variance. The estimated redshifts of the remaining 37 objects agree with the spectroscopic ones with an rms difference $\Delta z = 0.15$.

The surface density of high-redshift objects found by Steidel et al.[1], $0.40 \pm 0.07$ arcmin$^{-2}$ to magnitude $AB(6930) < 25$ at redshift $3 < z < 3.5$, is in good agreement with that found in our analysis, $1.2 \pm 0.5$ arcmin$^{-2}$. Furthermore, the surface densities reported in Table 1 decrease more or less monotonically with increasing redshift, which is in general accord with what is expected for distant galaxies due to luminosity distance and surface brightness effects but is not necessarily expected if the redshifts are generally in error.

We conducted two tests to verify that objects detected in the F814W image but not in the other images (and hence identified by the analysis at estimated redshift $z > 6$) are real and not due to noise fluctuations. First, we sought to identify spurious objects in the "negative" images, which were formed by reversing the sign of each pixel in the images. Using exactly the same procedures that were used on the positve images, we detected only three spurious objects of magnitudes $AB(8140) = 28.5 - 29.6$ in the negative images, of which only one is at "estimated redshift" $z > 6$, compared with 16 objects at $z > 6$ in the positive images, of which one, four, and 13 are of magnitude $AB(4500) < 27$, 28, and 29, respectively. This rules out spurious detections due to a symmetric noise distribution. To eliminate the possibility of spurious detections due to a skewed noise distribution, caused by noise added to weak sources below the detection limit, we repeated the analysis with the roles of the F814W and F450W images interchanged. (These two images have approximately the same limiting magnitude; this test cannot be conducted with the F606W image, which is almost a magnitude deeper.) As none of the spectra are expected to peak at 4,500 Å and be undetected at higher wavelengths, any detection with "estimated redshift" $z > 4$ would be spurious. The highest estimated redshift found in the test was, in fact, $z = 3.64$.

The spectra of the extreme objects at estimated redshift $z > 6$ are consistent with redshifted Lyman-limit absorption of high-redshift galaxies but inconsistent with many other interpretations, including lower-redshift galaxies, line-dominated galaxies, and heavily reddened lower-redshift galaxies. The brightest of these objects (object 1,668 in the full catalogue; see Supplementary Information) shows a $3\sigma$ lower limit of 12 to the F814W/F606W flux ratio, and the composite spectral energy distribution of these objects shows a $3\sigma$ lower limit of 20 to the F814W/F606W flux ratio. No other astrophysical object of which we are aware satisfies these constraints. Specifically, spec-

trophotometric atlases of galaxies[13,14] show no galaxy with a spectral decrement anywhere near a factor of 20 over any wavelength range that might be redshifted into the F814W and F606W images, and extreme line-dominated galaxies usually exhibit strong ultraviolet continuum radiation[15].

The possibility that the objects might be heavily-reddened low-redshift galaxies is unlikely on several accounts. First, three magnitudes of reddening, which corresponds to about 9 magnitudes of extinction in the F814W images, would be required to suppress the F606W images by a factor of 20 relative to the F814W images (assuming a reasonably flat unobscured spectrum). If it were heavily reddened, object 1,668 would have an unobscured magnitude of $AB(8140) = 26 - 9 = 17$, yet it is smaller than 1 arcsec. Second, if the objects were heavily reddened, then they would be very noticeable at longer wavelengths. Object 1,668 would be of magnitude $AB(19000) \approx 21 - 22$. Infrared images of the HDF area of the sky have been checked (L. Cowie, personal communication) and place an approximate, $1\sigma$, limit of $AB(19000) \gtrsim 25$ on this object, thus ruling out the possibility of heavy reddening in this case. Third, it is necessary to account for the surface density of the objects, that is, $\sim 1$ arcmin$^{-2}$. Odd, heavily reddened, nearby galaxies cannot serve as prototypes for the galaxies at estimated redshift $z > 6$ unless the density of such local galaxies can be shown to be high enough.

Even if the high-redshift estimates are incorrect, the results of the analysis can be used to set strict upper limits to the surface density of real high-redshift galaxies because such galaxies must exhibit the spectral signature of Lyman-limit and Ly$\alpha$-forest absorption and so must be identified by the analysis as high-redshift objects. Such galaxies would fail to be identified by the analysis as high-redshift galaxies only if they were blocked by bright, foreground galaxies or were incorrectly identified as low-redshift galaxies due to photometric uncertainties. To test both of these effects, we placed "synthetic" models of all the objects of magnitude $AB(8140) < 28$ (matching both the magnitudes and sizes of the real objects) at random locations within the images and sought to recover the redshifts by exactly the same analysis procedures used to identify the real galaxies. Figure 4 shows that the great majority of the objects are recovered at their input redshifts with an r.m.s. difference $\Delta z = 0.11$, similar to the redshift difference found between the estimated and spectroscopic redshifts. The remaining objects have discordant estimated redshifts due to photometric uncertainties and confusion with faint sources, but none have estimated redshifts $z > 5$. (Cosmic variance is not an issue since the simulated objects were modelled with the spectral energy distributions used in the analysis.)

Many of the objects, including some of those with highest estimated redshifts, are clearly spatially resolved, which excludes Galactic stars as possibilities. (Their spectra are, in any case, inconsistent with those of M stars.)

We therefore conclude that the redshifts are probably correct.

## Galaxies in the early universe

If the redshifts we have estimated are approximately correct, then the high-redshift objects typically have ultraviolet luminosities $\sim 10^9 - 10^{10} L_\odot$, sizes $\sim 1$ kpc, and co-moving spatial densities that vary between 0.05 and 0.01 Mpc$^{-3}$ at redshifts between $z = 2.5$ and $z = 6$. The luminosities and sizes are modest in comparison to luminous galaxies but are similar to those of nearby starbursting galaxies[16]. On the other hand, the co-moving spatial density of the objects is comparable to or even larger than that of luminous galaxies. The objects therefore appear to represent star formation in small, concentrated regions rather than in galaxy-sized objects. At the early epochs spanned by the objects, the dynamical timescale of galaxy-sized objects is comparable to the age of the universe, which suggests that we may be witnessing the first star formation associated with the initial collapse of galaxies. In fact, the rapid decline in surface density as a function of redshift for $z > 2$ severely constrains models for galaxy formation and evolution (A.Y., K.M.L., A. Campos, and A.F.-S., manuscript in preparation). In any event, we interpret the objects as galactic or proto-galactic regions of star formation associated with the progenitors of present-day normal galaxies at epochs reaching back 95% of the time to the Big Bang.

---

Received 7 March 1996; accepted 4 June 1996.

1. Steidel, C., Giavalisco M., Pettini M., Dickinson M. & Adelberger K. Astrophys. J. in press, Los Alamos preprint astro-ph/9602024 (1996).

2. Bertin, E. & Arnouts, S. Astr. Astrophys. Suppl. in press (1996).

3. Irwin, M. J. Mon. Not. R. astr. Soc. **214**, 575–604 (1985).

4. Coleman, G. D., Wu, C. C. & Weedman, D. W. Astrophys. J. Suppl. **43**, 393–416 (1980).

5. Kinney, A. L., Bohlin, R. C., Calzetti, D., Panagia, N. & Wyse, R. F. G. Astrophys. J. Suppl. **86**, 5–93 (1993).

6. Leitherer, C., Ferguson, H. C., Heckman, T. M. & Lowenthal, J. D. Astrophys. J. **454**, L19–22 (1995).

7. Lanzetta, K. M. Astrophys. J. **375**, 1–14 (1991).

8. Madau, P. Astrophys. J. **441**, 18–27 (1995).

9. Jacoby, G. H., Hunter, D. A. & Christian C. A. Astrophys. J. Suppl. **56**, 257–281 (1984).

10. Steidel, C., Giavalisco M., Dickinson, M. & Adelberger, K. L. Astr. J. in press, Los Alamos preprint astro-ph/9604140 (1996).

11. Cowie, L. L. http://www.ifa.hawaii.edu/∼cowie/hdf.html (1996).

12. Moustakas, L., Zepf, S., & Davis, M. http:////astro.berkeley.edu/davisgrp/HDF/ (1996).

13. Kennicutt, R. C. Astrophys. J. Suppl. **79**, 255–284 (1992).

14. Liu, C, T. & Kennicutt, R. C. Astrophys. J. Suppl. **100**, 325–346 (1995).

15. Thuan, T. X. in "Massive Stars in Starbursts", eds. C. Leitherer et al. (Cambridge: Cambridge University

Press), pp. 183–203 (1991).

16. Meurer, G. R., Heckman, T. M., Leitherer, C., Kinney, A., Robert, C. & Garnett, D. R. Astr. J. **110**, 2665–2691 (1995).

SUPPLEMENTARY INFORMATION. Available on *Nature's* World-Wide Web site http://www.-nature.com. Paper copies are available from Mary Sheehan at the London editorial office of *Nature*.

ACKNOWLEDGEMENTS. We are grateful to X. Barcons, A. Burrows, A. Campos, L. Cowie, J. Lattimer, D. Peterson, R. Puetter, M. Simon, P. Solomon, F. Walter, and J. Webb for fruitful discussions; E. Bertin, L. Cowie, R. Rebolo, and J. Webb for software and data used in the analysis; S. Zoonematkermani for assisting with graphical display of the HDF images, and to R. Williams and the staff of STScI for providing access to the reduced HDF images. This research was supported by NASA, the Dudley Observatory, a Spanish MEC studentship, and the Spanish DGICYT.

CORRESPONDENCE should be addressed to K.M.L. (email: lanzetta@sbastc.ess.sunysb.edu).

TABLE 1 Galaxy surface densities

| | Surface Density (arcmin$^{-2}$) | | | |
|---|---|---|---|---|
| $z$ | $AB(8140) < 25$ | $AB(8140) < 26$ | $AB(8140) < 27$ | $AB(8140) < 28$ |
| $0.0 - 0.5$ ..... | 7.1 (0.6) | 13.3 (0.9) | 22.0 (1.1) | 35.5 (1.4) |
| $0.5 - 1.0$ ..... | 20.4 (1.1) | 28.0 (1.3) | 39.1 (1.5) | 51.4 (1.7) |
| $1.0 - 1.5$ ..... | 13.0 (0.9) | 23.7 (1.2) | 42.7 (1.5) | 65.2 (1.9) |
| $1.5 - 2.0$ ..... | 8.3 (0.7) | 18.5 (1.0) | 34.6 (1.4) | 56.2 (1.8) |
| $2.0 - 2.5$ ..... | 2.1 (0.3) | 8.1 (0.7) | 15.2 (0.9) | 24.6 (1.2) |
| $2.5 - 3.0$ ..... | 0.9 (0.2) | 1.9 (0.3) | 3.1 (0.4) | 7.3 (0.6) |
| $3.0 - 3.5$ ..... | 1.2 (0.3) | 2.1 (0.3) | 4.5 (1.5) | 8.3 (0.7) |
| $3.5 - 4.0$ ..... | 0.2 (0.2) | 1.2 (0.3) | 2.6 (0.4) | 4.5 (0.5) |
| $4.0 - 4.5$ ..... | 0.2 (0.2) | 0.7 (0.2) | 2.8 (0.4) | 5.2 (0.5) |
| $4.5 - 5.0$ ..... | 0.2 (0.2) | 0.2 (0.2) | 0.5 (0.2) | 1.9 (0.5) |
| $5.0 - 5.5$ ..... | 0.0 (0.2) | 0.0 (0.2) | 0.2 (0.2) | 0.5 (0.3) |
| $5.5 - 6.0$ ..... | 0.0 (0.2) | 0.0 (0.2) | 0.0 (0.2) | 0.0 (0.2) |
| $> 6.0$ ..... | 0.0 (0.2) | 0.0 (0.2) | 0.2 (0.2) | 0.9 (0.2) |

Fig. 1.— Expected $AB$ magnitudes of the four galaxy types—E (solid), Sbc (dotted), Scd (short dashed) and Irr (long dashed)—through the WFPC2 filters for galaxies of absolute magnitude $M_{AB(4500)} = -20$ ($H_0 = 100$ km s$^{-1}$ Mpc$^{-1}$). The top panels are for $\Omega = 0$ and the bottom panels for $\Omega = 1$. The WFPC2 images are sensitive to galaxies at redshifts as large as $z \approx 7$, beyond which the Lyman limit is redshifted past the response of the F814W filter.

Fig. 2.— Sample spectral energy distributions (left panels) and redshift likelihood functions (right panels) of 24 objects of magnitude $AB(8140) < 28$. For the spectral energy distributions, vertical error bars show uncertainties, horizontal error bars show bin sizes, and solid curves show best-fit model spectral energy distributions. Rough uncertainties for the derived redshifts can be estimated by identifying the redshift regions over which the redshift likelihood functions exceed $\exp(-1/2)$ times the maximum-likelihood values. However, the redshift likelihood functions are, in general, quite complicated and often show multiple local maxima. Moreover, they do not take into account the cosmic variance. For these reasons, the uncertainties determined by this method provide only rough indications of the true uncertainties.

Fig. 3.— Redshifts estimated in this paper versus spectroscopic measurements by Steidel et al.[10] (solid circles), Cowie[11] (crosses), and Moustakas et al.[11] (open boxes). Of the 44 objects, three high-redshift galaxies have redshifts underestimated by $\Delta z \approx 1$, owing to confusion with the UV emission of other faint galaxies, and four bright ($AB(8140) = 20.5 - 22.8$) medium-redshift objects have redshifts overestimated by $\Delta z > 1$, because the uncertainties used in Equation (1) do not include the cosmic variance. The estimated redshifts of the remaining 37 objects agree with the spectroscopic ones to an r.m.s. difference $\Delta z = 0.15$.

Fig. 4.— Output redshifts $z_{\rm out}$ versus input redshifts $z_{\rm in}$ of the synthetic models of the objects. Of the 1,104 objects included into the simulation, 170 (or 15%) were by chance placed on or near other objects and showed a brightening of $\Delta AB(8140) > 0.15$. The 934 remaining objects were recovered with an r.m.s. difference $\Delta AB(8140) = 0.045$ between the input and output magnitudes. Of these, 97 (or 9% of the original sample) were identified by the analysis with redshift differences $z_{\rm in} - z_{\rm out} > 0.5$, with typical differences around 2. The remaining 837 (or 76% of the original sample) were identified at output redshifts essentially equal to the input redshifts, with an r.m.s. difference $\Delta z = 0.10$, which is comparable to that between the estimated redshifts and those measured by Steidel et al.[10], Cowie[11], and Moustakas et al.[12].

arXiv:astro-ph/9606171v1 27 Jun 1996

# Star-forming galaxies at very high redshifts
# Supplementary information

**Kenneth M. Lanzetta[1], Amos Yahil[1] & Alberto Fernández-Soto[2,3]**

[1]Astronomy Program, Department of Earth and Space Sciences, State University of New York at Stony Brook, Stony Brook, NY 11794–2100, USA

[2]Instituto de Física de Cantabria, Consejo Superior de Investigaciones Científicas, [3]Departamento de Física Moderna, Universidad de Cantabria, Facultad de Ciencias, 39005 Santander, SPAIN

---

This document presents supplementary information for an article published in the 27 June 1996 edition of *Nature*, 381, 759–763. The supplementary information is available electronically from ftp://ftp.ess.sunysb.edu/pub/hdf.

Table 1 (17 pages) lists the identification number, WFPC2 chip number, WFPC2 pixel coordinates $x$ and $y$ of the trimmed images, J2000 Right Ascension and Declination $\alpha$ and $\delta$, total magnitude $AB(8140)$, relative fluxes $f(3000)$, $f(4500)$, $f(6160)$, and $f(8140)$ (and uncertainties), and maximum-likelihood redshift estimate $z$ of the 1,683 objects identified by the analysis. Uncertainties are given in parenthesis. To obtain WFPC2 pixel coordinates of the Version 2 drizzled images, add 190 to both $x$ and $y$.

Figure 1 (38 pages) shows spectral energy distributions (left panels of each pair) and redshift likelihood functions (right panels of each pair) of the 1,683 objects identified by the analysis. For the spectral energy distributions, vertical error bars show uncertainties, horizontal error bars show bin sizes, and solid curves show best-fit model spectral energy distributions.

Figure 2 (1 page) shows optimally-added composite spectral energy distributions of the objects identified by the analysis at redshift $z > 2.5$. Vertical error bars show uncertainties and horizontal error bars show bin sizes. Vertical dashed lines indicate onset of the Lyman limit (shorter wavelengths) and the Ly$\alpha$ forest (longer wavelengths) at the midpoint of each redshift bin.